Available online at www.sciencedirect.com
ScienceDirect
Journal of Solid State Chemistry 181 (2008) 282–293
JOURNAL OF SOLID STATE CHEMISTRY
www.elsevier.com/locate/jssc

Crystal structures and magnetic properties of $CeAu_4Si_2$ and $CeAu_2Si_2$

Athena S. Sefat[a,b,*], Andriy M. Palasyuk[a,c], Sergey L. Bud'ko[a,b], John D. Corbett[a,c], Paul C. Canfield[a,b]

[a]*Ames Laboratory, Iowa State University, Ames, IA 50011, USA*
[b]*Department of Physics and Astronomy, Iowa State University, Ames, IA 50011, USA*
[c]*Department of Chemistry, Iowa State University, Ames, IA 50011, USA*

Received 7 September 2007; received in revised form 15 November 2007; accepted 25 November 2007
Available online 3 December 2007

Abstract

Single crystals of $CeAu_4Si_2$ and $CeAu_2Si_2$ have been grown out of ternary fluxes rich in Au, and the former, also by sintering the stoichiometric composition at 750 °C. The single-crystal X-ray refinement result for $CeAu_4Si_2$ is orthorhombic, *Cmmm* (No. 65, $Z = 2$), different from a tetragonal result found from an X-ray powder diffraction refinement [H. Nakashima, et al., J. Alloys Compds. 424 (2006) 7]. For $CeAu_2Si_2$, this is the first report of the stoichiometric crystalline phase, in the known tetragonal *I*4/*mmm* structure. The anisotropic field- and temperature-dependent magnetizations, as well as specific heat and resistivity data are compared. Although both compounds have related structural packing, they present unique magnetic features. $CeAu_2Si_2$ is a typical antiferromagnet with $T_N = 8.8(1)$ K and $CeAu_4Si_2$ features a ferromagnetic component below $T_c = 3.3(1)$ K. Both phases have effective moments close in value to that of free Ce^{3+}.
Published by Elsevier Inc.

Keywords: Flux growth; Single crystal; X-ray diffraction; $CeAu_2Si_2$; $CeAu_4Si_2$; Electrical resistivity; Magnetization; Specific heat

1. Introduction

Special interest is concentrated on the cerium-based ternary intermetallic compounds since they exhibit a wide variety of magnetic ground states, ranging from magnetically ordered, to heavy fermionic and sometimes superconducting, to non-magnetic. Being at the beginning of the lanthanide series, the $4f^1$ state for Ce^{3+} is sufficiently extended that it may be broadened by hybridization with neighboring orbitals. Thus, fluctuations between the Ce^{3+} and Ce^{4+} configurations on the same atom may occur by the exchange between the 4*f* level and the conduction band. When the Ce local moment survives to low temperatures, it generally adopts an antiferromagnetic ground state [1–4]. Low-temperature ground states with a ferromagnetic component are less common but not unknown; examples being CePdSb [5], $CeAgSb_2$ [6], CeAgGa [7], $CeGe_2$ [8], CeGaGe [9] and CeAuGe [10].

The cerium transition-metal (*T*) silicides CeT_2Si_2 have the tetragonal $ThCr_2Si_2$-type structure with space group *I*4/*mmm* [11], in which the cerium ions lie on a tetragonal 4/*mmm* site, in a simple body-centered sublattice. The magnetic properties among the CeT_2Si_2 family are determined by the competition between the indirect exchange interaction of Ce^{3+} ions, by the Ruderman–Kittel–Kasuya–Yosida (RKKY) interaction, and the effective suppression of the Ce^{3+} moments because of Kondo screening or valence fluctuations [12]. The intersite interaction temperature (T_{RKKY}) and Kondo temperature (T_K) depend on the magnetic exchange integral between the Ce^{3+} 4*f* local moments and conduction electrons, J_{sf}, and the density of conduction electron states at the Fermi level, $N(E_f)$, such that $T_{RKKY} \propto J_{sf}^2 N(E_f)$ and $T_{K\alpha} \exp(-1/J_{sf}N(E_f))$. Investigations over several decades of the interactions of structural and electronic properties of the CeT_2Si_2 series have revealed that the change of *T* from the middle of the transition-metal series towards the later

*Corresponding author at: Department of Physics and Astronomy, Iowa State University, Ames, IA 50011, USA. Fax: +1 515 294 6027.
E-mail address: asefat@ameslab.gov (A.S. Sefat).

0022-4596/$ - see front matter Published by Elsevier Inc.
doi:10.1016/j.jssc.2007.11.029

noble metals varies the cerium from intermediate valent IV (T = Ru) to trivalent (T = Au). Weak hybridization and the dominant RKKY interaction can lead to long-range magnetic order (T = Rh, Pd, Ag, Pt, Au), or the hybridization may prevail, with strong hybridization favoring a nonmagnetic, valence fluctuating state at low temperatures (T = Ru) [13–17]. Numerous studies on $CeAu_2Si_2$ have concluded that it orders antiferromagnetically [1,2,17–22] and the Kondo temperature is reported to be small ($T_K = 1.7$ K) [17] compared with T_N. However, the antiferromagnetic ordering temperature for polycrystalline samples have been inconsistent, varying over $T_N = 6.6$ K [21], 7.3 K [22], ~9 K [19], 9.6 K [2], to 10 K [1,17]. For single-crystal cases, only two off-stoichiometry samples have been studied. For a $Ce_{1.13}Au_{2.07}Si_{1.80}$ crystal composition, based on microprobe analysis, $T_N = 4$ K [19], and this increases to 8.1 K for $Ce_{0.93}Au_{2.07}Si_{2.04}$ Czochralski melt composition [18]. To address such contradictions, we have studied a stoichiometric $CeAu_2Si_2$ phase, as confirmed by single-crystal X-ray results.

Motivated by the properties of the CeT_2Si_2 family of compounds, our interest in the closely related cerium gold silicide ($CeAu_4Si_2$) arose following the first report of its synthesis, structure, and magnetic properties by Nakashima et al. [23]. This phase was found to be a ferromagnet with $T_c = 5.3$ K and 1.7 μ_B/Ce saturation moment. The Rietveld refinement of the powder X-ray diffraction (XRD) pattern yielded an evidently new tetragonal structure type ($P\bar{4}m2$) No.115, $a = 4.3304$ Å, $c = 27.409$ Å) with the local environment of Ce similar to that of $CeAu_2Si_2$, but with intervening double gold layers. However, the positional parameters reported appeared to contain some inconsistencies, and neither the atom displacement ellipsoid nor the Rietveld refinement parameters were given. Here we show from single-crystal X-ray data that the similarly grown $CeAu_4Si_2$ phase crystallizes instead in a known [24] but fairly rare, orthorhombic $CeRe_4Si_2$-structure type (*Cmmm*). We also present the thermodynamic and transport data on this single crystal and make an association between it and the related $CeAu_2Si_2$ phase.

This report presents the experimental details, followed by the discussion of crystal structure, anisotropic field- and temperature-dependent magnetization $M(H, T)$, specific heat $C(T)$ and resistivity $\rho(T)$ of both the 1:2:2 and 1:4:2, Ce:Au:Si phases. In the concluding section, a comparative analysis of the related $CeAu_4Si_2$ and $CeAu_2Si_2$ compounds is given, with respect to structures, thermodynamic and transport properties. Our investigation of $CeAu_4Si_2$ may lead to new interest in the system with general formula CeT_4X_2, with T = transition metal and X = Si, Ge, Sn.

2. Experimental details

2.1. Crystals grown by flux method

Single crystals of $CeAu_4Si_2$ and $CeAu_2Si_2$ phases were grown by the self-flux method [25] with the $CeAu_4Si_2$ growth being similar to those reported previously [23,26]. The typical crystal size from both was $\sim 7 \times 4 \times 1$ mm^3. In the preparation of crystals, high-purity elements (>99.9%) were used. For $CeAu_4Si_2$, a Ce:Au:Si composition of 0.07:0.75:0.18 was heated to 1150 °C under 0.5 atm argon and then cooled at 4.2 °C/h, followed by decanting of flux at 780 °C. The crystals were plate like and malleable with the [010] direction perpendicular to the plane of the plate. For $CeAu_2Si_2$, a Ce:Au:Si composition of 0.04:0.66:0.3 was heated to 780 °C and then cooled at 6.7 °C/h, followed by decanting of flux at 730 °C. The crystals were brittle, well formed plates with the [001] direction perpendicular to the plane of the plate.

2.2. $CeAu_4Si_2$ crystals from stoichiometric sintering

The high-purity elements (>99.9%) in the stoichiometric Ce:Au:Si = 1:4:2 mol ratio were sealed in a tantalum ampoule which was jacketed in an evacuated silica tube, heated at 1100 °C for 12 h, and quenched in cold water. The container was then annealed at 750 °C for 360 h and quenched again. The product was mainly separate soft malleable crystals, of a size suitable for XRD (<0.1 mm^3).

2.3. Structure determination of $CeAu_4Si_2$

The data were collected with the aid of a Bruker APEX SMART CCD-equipped X-ray diffractometer, with monochromated Mo$K\alpha$ radiation ($\lambda = 0.71073$ Å). Because of the malleability of $CeAu_4Si_2$, it was difficult to extract undistorted crystals, but after several attempts, reasonable crystals were mounted from the flux product and their quality confirmed by the Laue photography. A total of 1818 frames were collected at room temperature, with exposures of 20 s per frame. The reflection intensities were integrated with SAINT subprogram in the SMART software package [27]. The XPREP subprogram in the SHELXTL [28] software package was used for space group determination, in which systematic absences indicated *C*222, *Cmmm, Cmm*2 and *Amm*2 as possible space groups. Centrosymmetry of the lattice was clearly indicated by the intensity statistics ($<E^2-1> = 1.037$), and the structure was solved satisfactorily in *Cmmm*. To confirm this symmetry and stoichiometry, data were also collected from a $CeAu_4Si_2$ crystal grown by sintering process. This data set was similarly collected, reduced and refined in *Cmmm* to give somewhat lower final residuals. Streaking in the CCD frames was observed for samples from both sources, presumably because of distortion on mounting the crystals, but the amount was clearly less for the sintered product. The numerical refinement results were very similar for both.

To account for the degree of flux contamination in the flux-grown crystals for which magnetic properties were measured, the X-ray powder diffraction data were collected from a ground $\sim 7 \times 4 \times 1$ mm^3 size crystals. The powdered sample was mounted between Mylar sheets and the

diffraction pattern was collected with the aid of a Huber 670 Guinier Powder Camera, equipped with an area-sensitive detector and Cu$K\alpha$ radiation ($\lambda = 1.540598$ Å). The step size was set at 0.005°, and the exposure time was 30 min. These data collected for the ground crystals from the sintered and flux-grown batches were virtually identical except for two weak lines from elemental gold in the latter sample.

2.4. Phase determination of $CeAu_4Si_2$

Initially the powder diffraction data were collected, as described above. Subsequently, a single-crystal structural refinement was made on a small crystal, from the same batch, with the aid of a STOE (S2) image plate diffractometer and Mo$K\alpha$ radiation ($\lambda = 0.71073$ Å). Although $CeAu_2Si_2$ is not a new structure [11], the structure was refined with the SHELXTL program [28] for the purpose of confirming its stoichiometry.

2.5. Physical property measurements

All of the physical property measurements, described below were made on the same piece of flux-grown crystal of $CeAu_4Si_2$, or $CeAu_2Si_2$, with approximate dimensions of $0.5 \times 2 \times 3\,mm^3$.

DC magnetization was measured as a function of temperature and magnetic field using a Quantum Design Magnetic Property Measurement System. For a typical temperature sweep experiment, the sample was cooled to 1.8 K in zero-field cooled (ZFC), and data were collected warming from 1.8 K in an applied field. Then the sample was cooled in the applied field (FC), and the measurement repeated from 1.8 K. At temperatures above 150 K, data for the magnetization divided by applied field were fitted to the Curie–Weiss law $M/H = \chi = C/(T-\theta)$ in which C is the Weiss constant and θ is the paramagnetic Weiss temperature. If cerium is the only moment-bearing ion, the term C is related to the effective moment in paramagnetic state and the expected $\mu_{eff} = g_J[J(J+1)]^{1/2} = 2.54/Ce^{3+}$ ($J = 5/2$ and $g = 6/7$). The results of these analyses are summarized below.

For $CeAu_4Si_2$, the magnetization was measured both with field parallel to the b- (the pseudo-tetragonal) axis, and in the ac-plane. Such measurements are denoted as $M_{||b}$ and $M_{\perp b}$, respectively. Because of problems with handling the soft crystal, it was not possible to orient it within the ac-plane. But, we made several magnetization measurements in the plane and found the signal to be essentially isotropic. For $CeAu_4Si_2$, $M_{||b}$, $M_{\perp b}$, and a polycrystalline average of the data determined by $M_{poly} = \chi_{poly} = (\chi_{||b} + 2\chi_{\perp b})/3$, were fitted to the Curie–Weiss expression. The latter was done in an attempt to remove the effects of the crystalline electric field splitting, at least to the first order, from the effective moment and the Weiss temperature [29,30]. Because of a ferromagnetic component, isotherms in the vicinity of T_c were measured and used for the construction of an Arrott plot [31] in the form of M^2 vs. $H_{eff}M^{-1}$. H_{eff} estimates the effective field inside the sample and is found by subtracting the demagnetizing field H_d by applied field ($H_d = NM$, in which N is the demagnetizing factor dependent on sample shape).

For $CeAu_2Si_2$, the magnetization was measured with field parallel to the tetragonal c-axis and along the grown ab-plane, giving $M_{||c}$ and $M_{\perp c}$, respectively. For this compound, the polycrystalline average of the susceptibility data was also estimated, similar to the description above. The low temperature magnetization data are presented as the Fisher's $d(\chi T)/dT$, which is found to be proportional to the magnetic specific heat near an antiferromagnetic transition [32]. The high temperature magnetization data were fitted to the Curie–Weiss law, as described for $CeAu_4Si_2$ above.

The specific heat data were measured using a Quantum Design Physical Property Measurement System via the relaxation method. For $CeAu_2Si_2$, data were collected down to 1.8 K, and for $CeAu_4Si_2$, down to 0.4 K using a ^{3}He insert. The direct measurement of electronic γ and lattice β contributions was hampered by the low temperature magnetic orderings of cerium. However, such contributions can be estimated by a plot of C/T against T^2 above their respective transition temperatures. The value of the Debye temperature (θ_D) can then be subsequently calculated by $\beta = 12\pi^4 R/5\theta_D^3$.

Temperature-dependent electrical resistance measurements were also performed using the PPMS, AC Transport option, with a 16 Hz excitation current of 3 mA. The electrical contacts were placed on samples in standard 4-probe geometry, using Pt wires and silver epoxy (EPO-TEK H20E). The currents were run along the plate directions, i.e. within the ac- and ab-planes, for the $CeAu_4Si_2$ and $CeAu_2Si_2$ cases, respectively. Data were collected down to the same temperatures as for specific heat measurements. Residual resistivity ratios are defined as $RRR = \rho(300\,K)/\rho(1.8\,K)$.

3. Results and discussion

3.1. Structure

3.1.1. $CeAu_4Si_2$

The XRD pattern of the powdered flux-grown crystal, with minimal surface flux contamination, is shown in Fig. 1a (top). The powder diffraction on another piece of crystal, suffering from a more visible surface flux, is also shown in the inset of this figure. As it is noted, the three peaks labeled by asterisks increase in intensity providing evidence for a secondary crystalline phase, Au [33] from the flux. The three Bragg peaks, ~38.2°, 64.5° and 77.5° are at best traces in the X-ray powder pattern of the sample prepared by stoichiometric sintering, shown in Fig. 1a (bottom).

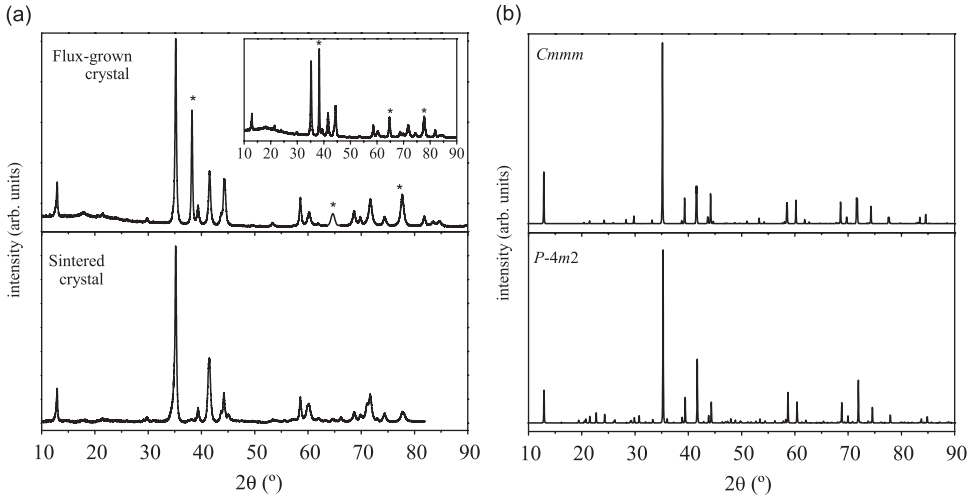

Fig. 1. (a) X-ray diffraction data of powdered $CeAu_4Si_2$ flux-grown crystal (top) and sintered crystal (bottom). The inset is the diffraction data of another piece of crystal, with visible surface flux. The asterisks indicate impurity Bragg peaks, according to *Cmmm* structure. (b) $CeAu_4Si_2$ simulated structure based on both of the space groups *Cmmm*, for the atomic coordinates presented in the text (top), and $P\bar{4}m2$ in Ref. [23] (bottom).

The malleability of $CeAu_4Si_2$ causes line broadening in the powder patterns because the lattice distortions generate small interplanar distance variations from point to point in the crystal grains. In the recent Nakashima et al. [23] publication a comparable broadening effect on the Bragg peaks was also evident. They reported that $CeAu_4Si_2$ was tetragonal ($P\bar{4}m2$, No. 115, $a = 4.3304$ Å, $c = 27.409$ Å) on the basis of Rietveld refinement of the powder diffraction data. The simulated powder patterns for our *Cmmm* result (as is described below) and their $P\bar{4}m2$ (result [23]) are compared in Fig. 1b. The two calculated patterns are quite similar on this scale, although the differences do appear to be distinctive in the $2\theta = 20$–32° range. However, the precise numerical powder data cannot be fitted to tetragonal symmetry. But in order to confirm the novel structural details, we have refined our single-crystal XRD data from the 1:4:2 crystals from both sources.

The softness of $CeAu_4Si_2$ is evidently also responsible for some broadening of single-crystal diffraction peaks in the form of streaks. Despite this difficulty, the structure was solved satisfactory from two small crystals from the flux grown and sintered batches. $CeAu_4Si_2$ is found to crystallize in a rare *Cmmm* structure type (No. 65, $a = 4.316(2)$ Å, $b = 13.741(8)$, $c = 4.350(2)$ Å) first determined from single-crystal data for $CeRe_4Si_2$ and afterwards confirmed for $PrRe_4Si_2$ [24].

The full-matrix least-squares refinement data from the sintered crystal converged at $R(F) = 3.36\%$, $wR_2 = 8.64\%$ for data with $I/\sigma(I) > 2$, whereas the flux-grown crystal data gave values about two percent higher for each. The largest positive and negative residuals in the ΔF map were 4.74 and -3.42 Å^{-3}, respectively, and all atom positions were fully occupied. The 2*a* Ce position refined to a 93(3) at% occupancy with the flux-grown crystal data, which is statistically marginal, and for simplicity it will continue to be noted as $CeAu_4Si_2$. Otherwise the positional and ellipsoidal parameters and the distances were substantially the same for both refinements. Some data collection and refinement parameters are listed in Table 1. Table 2 gives the atomic positions and equivalent displacement parameters, and Table 3 lists important interatomic distances for both $CeAu_2Si_2$ and the former $CeAu_4Si_2$. The CIF files for all three refinements have been deposited. There is of course no doubt that the measured positions of ~1020 single-crystal diffraction peaks observed for $CeAu_4Si_2$ are consistent with the orthorhombic cell and not the tetragonal lattice reported earlier [23].

Table 1
Crystal and structure data parameters for flux-grown $CeAu_2Si_2$ and sintered $CeAu_4Si_2$

Formula	$CeAu_2Si_2$	$CeAu_4Si_2$
Formula weight	590.23	974.36
Crystal system	Tetragonal	Orthorombic
Space group (no.), *Z*	*I*4/*mmm* (139), 2	*Cmmm* (65), 2
Unit cell dimensions		
a (Å)	4.3072(6)	4.316(2)
b (Å)	–	13.741(8)
c (Å)	10.196(2)	4.350(2)
V (Å^3)	189.15(5)	258.0(4)
$d_{calc.}$ (Mg/m^3)	10.36	12.67
μ(MoKα) (mm^{-1})	89.6	122.2
Total no. of reflections	1584	1023
Independent reflections	168 [$R_{int} = 0.0952$]	208 [$R_{int.} = 0.0650$]
Reflections with $I > 2\sigma(I)$	150	169
Goodness-of-fit on F^2	1.115	1.180
Final *R* indices		
R_1, wR_2 [$I > 2\sigma(I)$]	0.0562, 0.1253	0.0336, 0.0854
Largest diff. peak and hole	5.01 and −5.93	4.74 and −3.42

The structure of $CeAu_4Si_2$ can be described in terms of layers of distorted tetragonal antiprisms [$SiCe_4Au_4$] connected to each other by two faces of cerium atoms (Fig. 2a). The cerium point symmetry is orthorhombic (*mmm*). The stacking of layers of distorted square

Table 2
Atomic coordinates and equivalent isotropic displacement parameters ($Å^2 \times 10^3$) for $CeAu_2Si_2$ and $CeAu_4Si_2$

Compound	Atom	Wyckoff	x	y	z	$U_{eq.}$	Occup.
$CeAu_2Si_2$	Ce	2*b*	0	0	1/2	10(1)	1.02(2)
	Au	4*d*	0	1/2	1/4	14(1)	0.99(2)
	Si	4*e*	0	0	0.1133(7)	12(1)	1.01(2)
$CeAu_4Si_2$							
	Ce	2*a*	0	0	0	8(1)	0.98(2)
	Au1	4*j*	0	0.1774(1)	1/2	11(1)	1.01(2)
	Au2	4*i*	0	0.3230(1)	0	9(1)	0.99(2)
	Si	4*j*	0	0.4155(9)	1/2	15(1)	1.01(2)

Table 3
Important bond lengths (Å) in $CeAu_2Si_2$ and $CeAu_4Si_2$

$CeAu_2Si_2$		$CeAu_4Si_2$		$\sum$(PB)[a]
Atoms	*d*	Atoms	*d*	
Ce–Si × 8	3.257(3)	Ce–Si × 4	3.277(5)	3.00
Ce–Au × 4	3.3369(4)	Ce–Au1 × 4	3.267(3)	3.26
		Ce–Au2 × 4	3.252(3)	
Au–Si × 4	2.565(4)	Au1–Si × 2	2.508(7)	2.61
		Au2–Si × 2	2.520(7)	
Au–Au × 4	3.0457(4)	Au1–Au1 × 2	2.939(4)	2.88
		Au1–Au2 × 2	2.955(3)	
		× 4	3.064(3)	
		Au2–Au2 × 2	2.946(4)	
Si–Si	2.31(1)	Si-Si	2.32(2)	2.34

[a]Pauling single bond radii sum; Ref. [36].

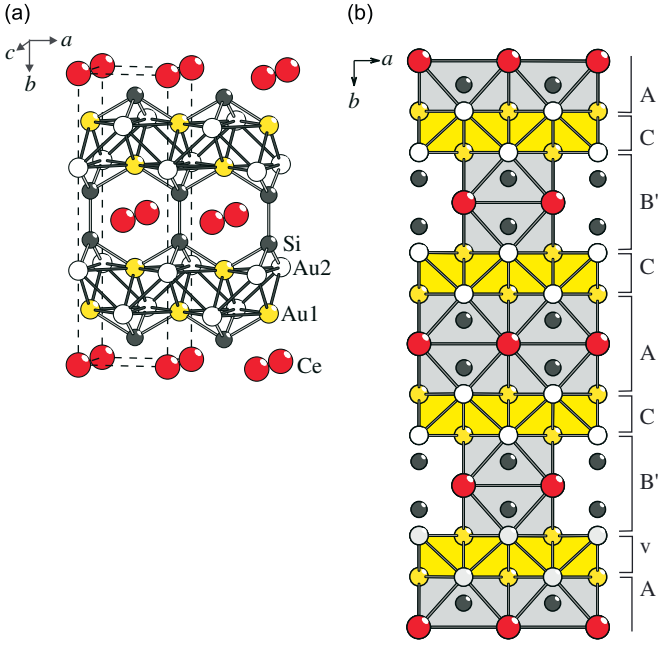

Fig. 2. (Color online) (a) Crystal structure of orthorhombic $CeAu_4Si_2$ (*Cmmm*), (b) with stacking of layers of condensed tetragonal antiprisms and gold layers. Ce, Au and Si atoms are in gray, white and black, respectively.

antiprisms and their separation by layers of empty gold octahedra [Au_6] along the [010] direction are shown in Fig. 2b. Because of the *c*-centering in $CeAu_4Si_2$, every second layer of distorted antiprisms cannot satisfy a hexagonal-close-packed (hcp) sequence; rather it is shifted in the [110] plane by $a/2$ with respect to previous layer, not by $a/2$ and $b/2$ required for hcp.

3.1.2. *$CeAu_2Si_2$*

$CeAu_2Si_2$ was discovered by Mayer et al. in 1973 [11] and characterized by X-ray and neutron powder diffraction data. It crystallizes with structure type $ThCr_2Si_2$, an ordered ternary variant of $BaAl_4$ (*I*4/*mmm*, No. 139), as described by Häussermann et al. [34]. The powder XRD pattern is shown in Fig. 3, along with the simulated pattern for *I*4/*mmm*. The data compare well, but there is evidence of a crystalline secondary phase (marked with asterisks at 38.2°, 64.5°, 77.5°), consistent with Au flux impurity.

The single-crystal XRD measurements were made to establish the stoichiometry. The details for this are listed in Table 2; the structure is ordered, with full occupancies of Ce, Au and Si sites within one standard deviation. The structure of $CeAu_2Si_2$, similar to the $BaAl_4$ description, can be characterized as a three-dimensional (3D) network of ${}^3_\infty[Au_2Si_2]^{3-}$ polyanion, with cerium atoms at the center and corners of the body-centered tetragonal unit cell (Fig. 4a) and encapsulating the Si and Au polyhedra. In

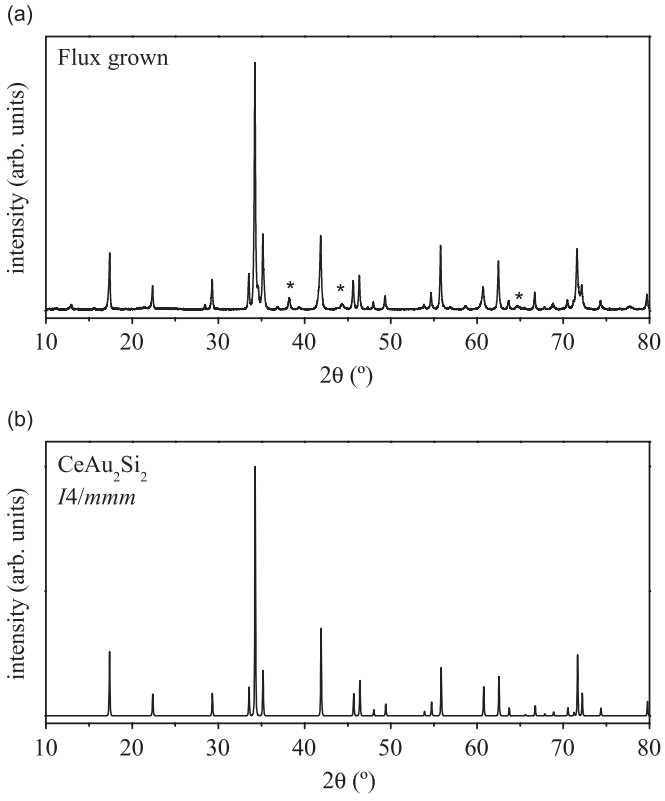

Fig. 3. (a) X-ray powder diffraction data for flux-grown $CeAu_2Si_2$ crystal, (b) the structural simulation of the refined *I*4/*mmm* structure. The asterisks in (a) mark impurity Bragg peaks.

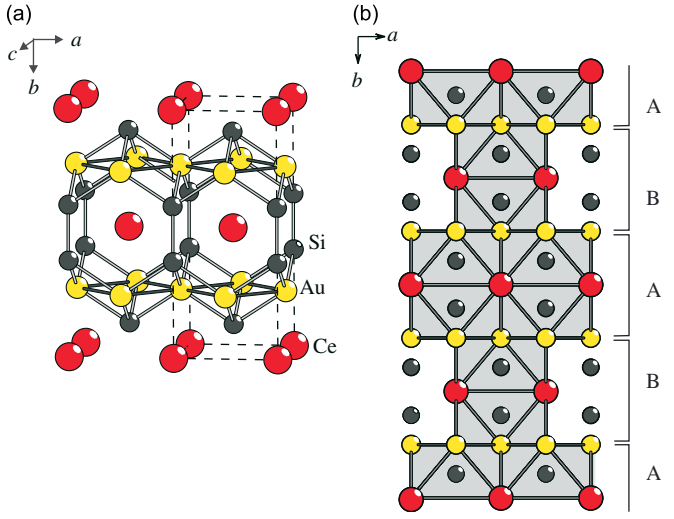

Fig. 4. (Color online) (a) Crystal structure of orthorhombic $CeAu_2Si_2$ ($I4/mmm$), (b) stacking of layers of condensed tetragonal antiprisms. Ce, Au and Si atoms are in gray, white, and black, respectively.

contrast to the $BaAl_4$ type of structure, in which both basal 4*d* (1/2, 0, 1/4) and apical 4*e* (0, 0, *z*) Wyckoff sites are occupied by Al, in $CeAu_2Si_2$ the 4*d* and 4*e* positions contain Au and Si atoms, respectively. Thus the two-dimensional (2D) square nets are constructed from Au atoms and are alternately capped above and below the plane by Si atoms to generate infinite 2D square pyramidal units defined by Si–Si bonds. The coordination polyhedra of Ce is tetragonal ($4/mmm$). The structure of $CeAu_2Si_2$, similar to that of $CeAu_4Si_2$, can be described in terms of layers of distorted tetragonal antiprisms [$SiCe_4Au_4$] centered by Si atoms, connected to each other through the common square faces [Ce_4] and stacked along [001] with a sequence ABAB (Fig. 4b).

3.2. Physical properties

3.2.1. $CeAu_4Si_2$

The magnetization of the orthorhombic $CeAu_4Si_2$ as a function of temperature in an applied field of 100 Oe is displayed in Fig. 5a. The crystallographic *b*-direction is the magnetic easy axis, with an order of magnitude larger magnetization at 1.8 K, compared with the perpendicular direction. For $M_{\|b}$, two magnetic features are evident at ~3.5 and 2 K, and for $M_{\perp b}$ there is one at ~3.5 K (Fig. 5a, inset). There is a divergence between ZFC and FC data below ~4 K. This feature suggests a ferromagnetic component. The report on the supposed stoichiometric and tetragonal $CeAu_4Si_2$ crystal gave $T_c = 5.3$ K, estimated from $M(T)$ under an applied field of 20 kOe, $\rho(T)$ and $C(T)$ [23].

The inverse of magnetization data follows the simple Curie–Weiss behavior between 200 and 300 K (Fig. 5b). Below this region, the magnetization deviates in both measured directions. This may be an influence of crystalline electric field splitting of Ce^{3+} ground state and a thermally induced change of the 4*f* electron level occupancy. The Curie–Weiss fits give $\mu_{eff(\|b)} = 2.33$ and $\mu_{eff(\perp b)} = 2.88\,\mu_B$/Ce with $\theta_{\|b} = 35(2)$ K and $\theta_{\perp b} = -52(2)$ K (Table 4). The polycrystalline averaged data are linear in temperature over a much larger range and manifest $\mu_{eff(poly)} = 2.65\,\mu_B$/Ce,

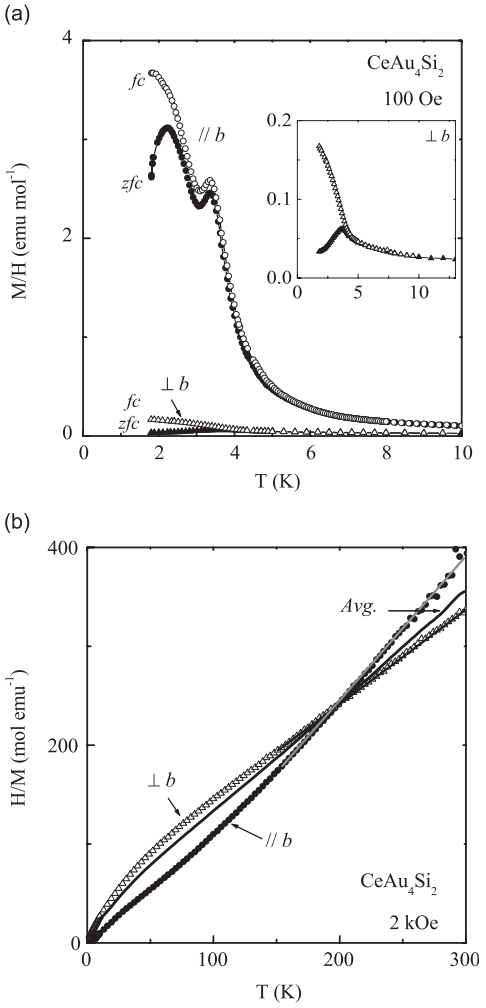

Fig. 5. Magnetization along two crystallographic directions for $CeAu_4Si_2$. (a) The temperature dependence of magnetization in zero-field cooled (ZFC) and field-cooled (FC) forms at 100 Oe and (b) the dependent of inverse magnetization, with fits to simple Curie–Weiss above 150 K. The inset in (a) is the enlarged $M_{\perp b}$ data.

Table 4
Paramagnetic effective moment (μ_{eff}) and Weiss temperature (θ) found by simple Curie–Weiss fit above ~150 K of the $M(T)$ data measured at an applied field of 2 kOe. The moments (μ) found at 1.8 K and 7 kOe are also listed. The χ_{poly} represents the polycrystalline averaged magnetization data (see text)

	$CeAu_4Si_2$			$CeAu_2Si_2$		
	$\|\| b$	$\perp b$	χ_{poly}	$\|\| c$	$\perp c$	χ_{poly}
μ_{eff}/Ce (μ_B)	2.33	2.88	2.65	2.54	2.46	2.49
θ(K)	35(2)	−52(2)	−15(2)	16(2)	−62(3)	−12(1)
μ/Ce (μ_B)	1.40	0.84	–	1.25	0.21	–

exceeding the free ion Ce^{3+} value (2.54 μ_B) by ~4%, and give $\theta_{poly} = -15(2)$ K. Our values are roughly analogous to those reported on the supposed tetragonal $CeAu_4Si_2$ phase with $\theta_{\|a} = 50$ K and $\theta_{\|c} = -94$ K [23], but without the anisotropy change above ~225 K.

The field-dependent magnetization isotherms for $CeAu_4Si_2$ exhibit a strong anisotropy, with a larger moment along b (Fig. 6). The magnetization curve along this axis rapidly rises to 0.69 μ_B/Ce by ~1 kOe, and continues to rise more gradually (Fig. 6, inset) giving a magnetic moment of 1.34 μ_B/Ce in 60 kOe. This saturated moment is not the full gJ value for the free ion (2.14 μ_B/Ce), perhaps owing to crystal field interactions. At 3 K, the saturated moment is slightly lower and 1.3 μ_B/Ce. The field-dependent magnetization perpendicular to b rises more slowly, reaching 0.84 μ_B/Ce by 70 kOe. The $M(H)$ in the ac-plane is found to be isotropic. The report on the tetragonal $CeAu_4Si_2$ gave a comparable saturation value of 1.7 μ_B/Ce along the easy axis, but a reduced 0.32 μ_B/Ce along the hard axis [23].

Given the apparent ferromagnetic nature of the upper transition in $CeAu_4Si_2$, more detailed magnetization data are required to infer an ordering temperature. To this end, isotherms in this vicinity have been measured (Fig. 7, inset) and used for the construction of an Arrott plot [31] in the form of M^2 vs. $H_{eff}M^{-1}$ (Fig. 7). Demagnetization correction of 0.9 kOe/μ_B was used ($N = 1$). In the limit of ZF, the line passing through the origin is 3.3 K, giving an estimate of the ferromagnetic ordering temperature. As will be discussed below, this value is consistent with the anomalies in specific heat data.

The transition to long-range magnetic order for $CeAu_4Si_2$ is seen in the ZF specific heat data, Fig. 8, as a rise in specific heat below 5 K followed by two magnetic anomalies at ~3.3 and 1.85 K (inset). The C/T vs. T^2 plot (Fig. 9a) follows a straight line for the region of ~8–15 K, just above the transition temperatures, which allows the estimation of $\gamma = 10(2)$ mJ/K^2 mol and ($\beta = 0.0033(1)$ mJ/K^4 mol) $\theta_D \approx 85$ K. The small value of γ indicates that

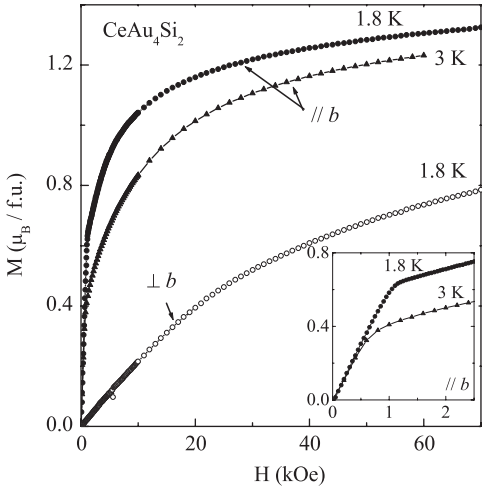

Fig. 6. For $CeAu_4Si_2$, magnetization vs. applied field along two crystallographic directions. Inset is the enlarged low field region for $M_{\|b}$.

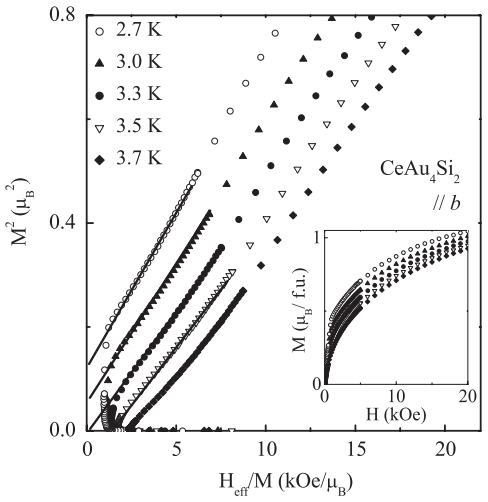

Fig. 7. For $CeAu_4Si_2$ and along the easy b-axis, the Arrott plot of M^2 vs. $H_{eff}M^{-1}$ is shown in which H_{eff} is the estimated effective field. Inset is the field-dependence of magnetization isotherms.

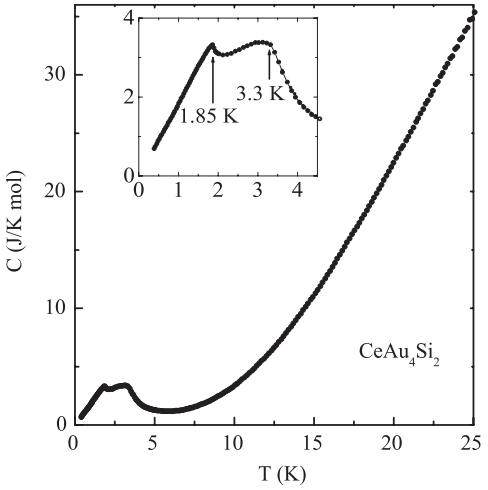

Fig. 8. For $CeAu_4Si_2$, temperature dependence of specific heat between 0.4 and 25 K. Inset is the enlarged low-temperature region.

the conduction electrons have little or no f character. This electronic specific heat coefficient is smaller than that reported previously for the tetragonal $CeAu_4Si_2$ ($\gamma = 24$ mJ/K^2 mol with $T_c = 5.3$ K) [23].

In order to obtain the magnetic specific heat, C_{mag}, the non-magnetic contributions ideally should be subtracted from measured specific heat. Here, the non-magnetic contributions are estimated from the γ and β values, and extrapolated below 8 K using $C(T) = \gamma T + \beta T^3$; this is shown as the dashed curve in Fig. 9b. The magnetic entropy, S, was then found by integration of C_{mag}/T vs. T (Fig. 9b inset). The entropy released up to the critical ordering temperature is ~$R \ln 2$, which implies a doubly degenerate ground state for $CeAu_4Si_2$. Data for the reported tetragonal $CeAu_4Si_2$ gave a slightly reduced $0.75R \ln 2$ at T_c (5.3 K) [23].

For $CeAu_4Si_2$, the temperature-dependent resistivity drops below 5 K (Fig. 10) presumably because of the loss

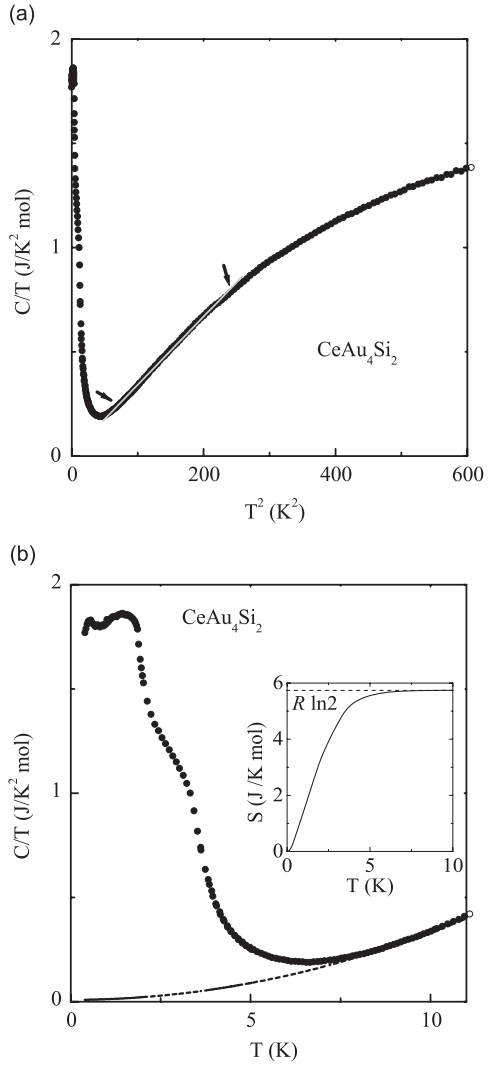

Fig. 9. For $CeAu_4Si_2$, specific heat data are shown in different forms: (a) C/T vs. T^2 and a linear fit in the range of ~8–15 K, shown by arrows; (b) C/T vs. T with the estimated non-magnetic contributions (of $\gamma T+\beta T^3$) in dashed curve below 10 K. Inset of (b) depicts the estimated magnetic entropy as a function of temperature.

of spin-disorder scattering in the ordered state. For the reported tetragonal $CeAu_4Si_2$ [23], a kink was noticed at 5.3 K (T_c). For $CeAu_4Si_2$, the residual resisitivity ratio is 2 and the room temperature resistivity is $\cong 65\,\mu\Omega$/cm.

3.2.2. *CeAu$_2$Si$_2$*

The magnetization as a function of temperature for $CeAu_2Si_2$ crystal is displayed in Fig. 11a. Along c, magnetic ordering is clearly visible below 9 K. At this temperature, $M_{\parallel c}\sim 7M_{\perp c}$. The peak at 9 K, with no difference between the ZFC and FC data, suggests antiferromagnetic nature. In literature, various Néel ordering temperatures, from 6.6 to 10 K [1,2,17,20–22], have been reported for polycrystalline samples. Moreover, for Czochralski-grown single crystals, Néel temperatures < 10 K were found, highly dependent on compositional variation along the length of the grown crystal [18,19].

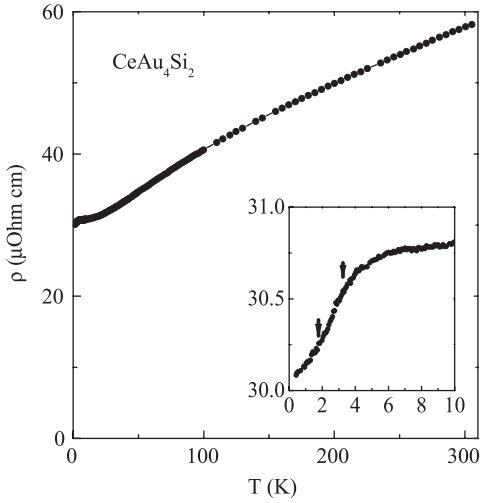

Fig. 10. For $CeAu_4Si_2$, the temperature dependence of resistivity. The location of anomalies from specific heat data are shown by arrows in the inset.

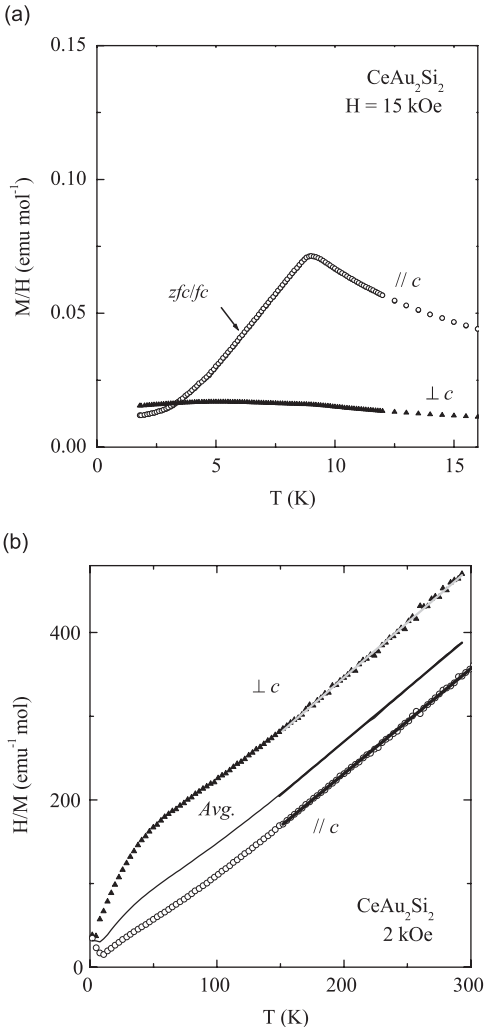

Fig. 11. For $CeAu_2Si_2$, the magnetization is measured along the two crystallographic directions. (a) The temperature dependence of magnetization is shown in zero-field cooled (ZFC)/field cooled (FC) forms at 15 kOe. (b) The temperature dependence of inverse magnetization is given, along with fits to Curie–Weiss above 150 K.

For $CeAu_2Si_2$, the inverse $M(T)$ data follow a Curie–Weiss behavior above ~150 K (Fig. 11b). Below this region; however, the magnetization shows deviation, especially for $M_{\perp c}$. The polycrystalline averaged data follow a Curie–Weiss behavior to much lower temperature. These data are consistent with crystalline electric field splitting of ground state of Ce^{3+} moment, with the moment being confined along the c-axis. For $CeAu_2Si_2$, the derived effective moment is $\sim 2.5\,\mu_B$, equal for both measured directions (Table 4). Cerium in this compound has a magnetic moment corresponding to the trivalent state, as μ_{eff} is close to the free ion value ($2.54\,\mu_B$). The paramagnetic Weiss temperatures are $\theta_{\parallel c} = 16(2)$ K, $\theta_{\perp c} = -62(3)$ K and $\theta_{poly} = -12(1)$ K. For different $CeAu_2Si_2$ compositions, previous studies have shown varying effective moments and Curie temperatures. For example for $Ce_{0.93}Au_{2.07}Si_{2.0}$ melt composition (T_N = 8.1 K), the reported values are $\mu_{eff} = 2.4\,\mu_B$, $\theta_{\parallel c} = 40$ K and $\theta_{//a} = -30$ K [18]. For $Ce_{1.13}Au_{2.07}Si_{1.8}$ Czochralski melt composition ($T_N = 4$ K), $\mu_{eff} \sim 2.57\,\mu_B$, $\theta_{\parallel c} = 25$ K and $\theta_{\parallel a} = -26$ K [19].

The field-dependent magnetization for $CeAu_2Si_2$ at 1.8 K is very anisotropic for $H > 50$ kOe (Fig. 12). Along c, the $M(H)$ first increases gradually with increasing field, and then exhibits a sharp metamagnetic transition at 46 kOe, reaching $1.3\,\mu_B$/Ce by 50 kOe. This saturation magnetization is quite small in comparison with that of the free Ce^{3+}, and may be due to crystal field splitting or a residual antiferomagnetic component in the higher field state. Previous $M_{\parallel c}$(H) data (on a crystal with $T_N = 8.1$ K) have shown a broader metamagnetic transition at 42 kOe, saturating at a comparable $1.35\,\mu_B$/Ce by 70 kOe [18]. For $Ce_{1.13}Au_{2.07}Si_{1.80}$ ($T_N = 4$ K), the metamagnetism is barely visible at ~20 kOe [19]. In the ab plane, the $M_{\perp c}$ data were found to increase weakly with increasing field and reaches $0.2\,\mu_B$/Ce at 70 kOe (Fig. 12), similar to the reported $0.25\,\mu_B$/Ce value [18].

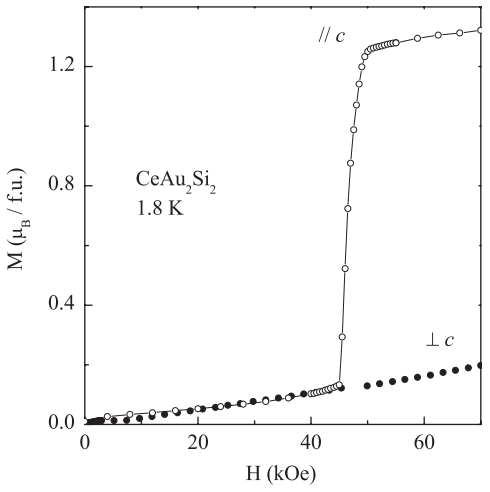

Fig. 12. For $CeAu_2Si_2$, the magnetization vs. applied field along two crystallographic directions.

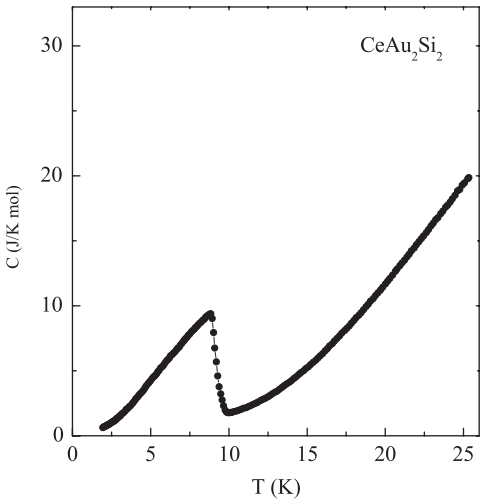

Fig. 13. For $CeAu_2Si_2$, temperature dependence of specific heat.

The specific heat result for $CeAu_2Si_2$ is displayed in Fig. 13. A pronounced anomaly is seen below ~10 K supporting the notion of a magnetic phase transition. The specific heat peak at 8.8 K is ascribed to the value of Néel temperature. In literature, $C(T)$ are reported with anomalies at 4 K [19], 7.3 K [22], and ~9 K [20].

For this compound, the C/T vs. T^2 plot (Fig. 14a) follows a straight line for a region just above the transition temperature, in the range of 10–18 K. The γ coefficient is 21(1) mJ/K^2 mol and from the slope ($\beta = 0.0015(1)$ mJ/K^4 mol) we infer $\theta_D \approx 110$ K. These values are comparable to that reported for the off stoichiometric $Ce_{1.13}Au_{2.07}Si_{1.80}$ crystal ($T_N = 4$ K): $\theta_D = 117$ K and $\gamma = 22$ mJ/K^2 mol [19]. For $CeAu_2Si_2$ polycrystal ($T_N = 7.3$ K), however, values of $\theta_D = 203$ K and $\gamma = 2.7$ mJ/K^2 mol were noted [22].

To obtain the magnetic specific heat for $CeAu_2Si_2$, nonmagnetic contributions are found from the lattice and electronic estimates and extrapolated below 10 K by generating points using $C(T) = \gamma T + \beta T^3$. This is shown by the dashed curve in Fig. 14b, and it is subtracted from measured specific heat. The magnetic entropy is then obtained by integrating C_{mag}/T vs. T, shown in Fig. 14b, inset. The entropy released up to the critical ordering temperature is $R \ln 2$, which implies a double degenerate ground state for $CeAu_2Si_2$. From neutron-scattering work, the ordered moment of Ce is $1.29(5)\,\mu_B$, a value that may correspond with the lowest doublet state [1]. Previously for a polycrystal sample ($T_N = 7.3$ K), a molar entropy of $\sim R \ln 2$ was given [22].

The temperature dependence of electrical resistivity, $\rho(T)$, for $CeAu_2Si_2$ is displayed in Fig. 15. It shows metallic behavior with a residual-resistivity ratio of ~2.3. In literature and for Czochralski grown $CeAu_2Si_2$ crystal, a RRR of 1.3 was reported [19]. The $\rho(T)$ (Fig. 15) initially decreases almost linearly with decreasing temperature down to ~150 K, shows a broad feature between 150 and ~50 K, and upon further cooling, gives a peak below 9 K (inset). This anomaly may be associated with

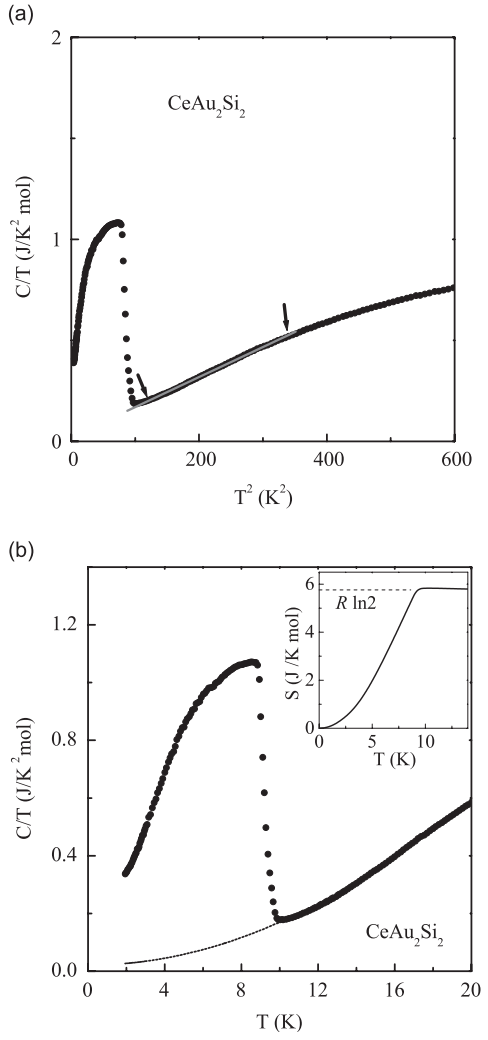

Fig. 14. For $CeAu_2Si_2$, data are shown (a) in the form of C/T vs. T^2 and linear fit between ~10 and 18 K and (b) C/T vs. T, with the estimate of non-magnetic contribution (of $\gamma T+\beta T^3$) as the dashed curve. The inset of (b) depicts the estimated magnetic entropy as a function of temperature.

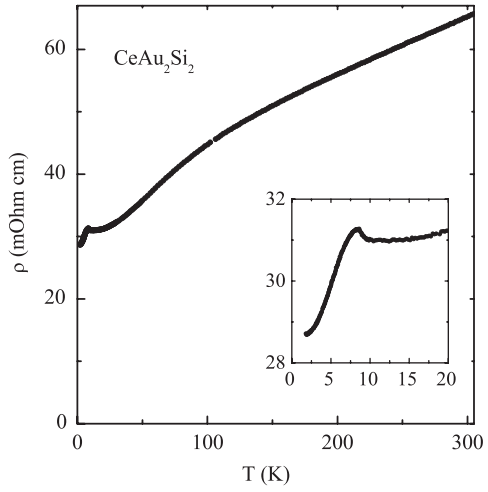

Fig. 15. For $CeAu_2Si_2$, the temperature dependence of resistivity is shown, with the enlarged low-temperature data in the inset.

antiferromagnetic correlations. The $\rho(T)$ curve here resembles that reported for $Ce_{1.13}Au_{2.07}Si_{1.80}$, but for the latter, a peak at 4 K was evident (T_N of this off-stoichiometric sample) [19].

For $CeAu_2Si_2$, the polycrystalline averaged magnetization data (Fig. 11a) manifests a sharp rise in $d(\chi T)/dT$ below 9 K (Fig. 16), peaking at 8.7 K. The specific heat data shows an anomaly below 10 K, peaking at 8.9 K. The derivative of resistivity, $d\rho/dT$, also manifests a peak at 9 K. As a result, the Néel temperature for this stoichiometric sample is found to be 8.8(1) K.

For $CeAu_2Si_2$, due to a small ferromagnetic impurity, weak isotropic hystereses are observed for $M_{\parallel c}$ and $M_{\perp c}$, at 1.8 K (Fig. 17a). The ordering temperature for this ferromagnetic phase is ~6 K, found as the divergence between the ZFC and FC $M(T)$ data, in a small applied field of 100 Oe (Fig. 17b). This is probably a contamination of a phase (non-crystalline), as we find variation in the

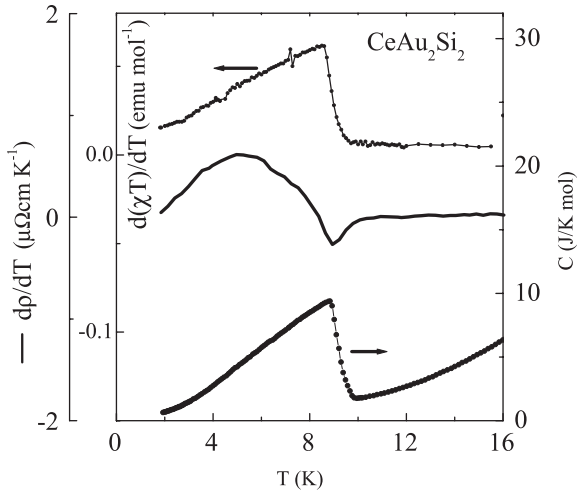

Fig. 16. For $CeAu_2Si_2$, the temperature dependence of specific heat is shown along with the average susceptibility form of $d(\chi T)/dT$ ($H = 1.5$ kOe) and also the derivative in resistivity, $d\rho/dT$.

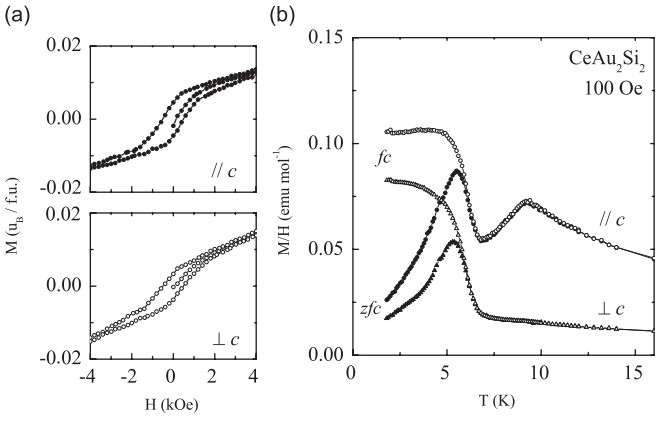

Fig. 17. For $CeAu_2Si_2$, an impurity ferromagnetic phase contributes to hysteresis at low fields (a), and zero-field cooled (ZFC)/field-cooled (FC) divergence below ~6 K (b). The measurements are done with applied field along two crystallographic directions.

magnitude of low temperature magnetization divergence in two slightly different grown batches. The T_c is consistent with that for $CeSi_x$ ($x \sim 1.84$) ordering below ~6.5 K [35]. It should be noted that the ferromagnetic impurity phase, with transition at ~6 K suggested by low-field $M(T)$ data is not visible in $C(T)$. Also, there is no anomaly at ~6 K in $\rho(T)$.

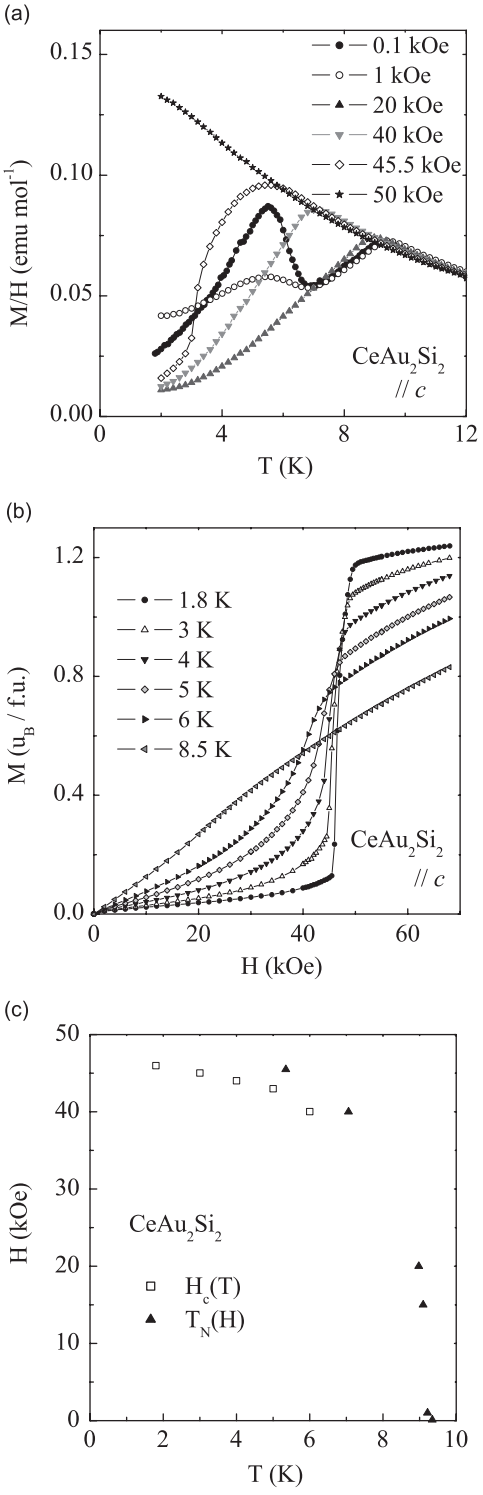

Fig. 18. (a) For $CeAu_2Si_2$, the zero-field cooled magnetization vs. temperature is shown at chosen applied fields along c-axis. (b) For $CeAu_2Si_2$, magnetization isotherms below $T_N \sim 8.8$ K are shown. (c) The H–T phase diagram represents the behavior of Néel temperature with applied field and also the dependence of critical metamagnetic transition (H_c) with temperature (results of dM/dH vs. H plots).

In Fig. 18a, the temperature dependence of magnetization was examined with increasing applied field, along c. The ferromagnetic component at ~6 K is reduced in magnitude in 15 kOe, and disappears in 20 kOe. With increasing field, the intrinsic antiferromagnetic transition of $CeAu_2Si_2$ at ~9 K shifts to lower temperatures. In 45.5 kOe the transition is rounded and by 50 kOe, the sample is completely forced into a field stabilized paramagnetic state. In Fig. 18b, the field-dependent magnetization isotherms, below Néel ordering temperature, are shown. The critical field (H_c) at 46 kOe and 1.8 K becomes less defined and broadened, shifting to lower fields, with increasing temperature. At 8.5 K, H_c is no longer visible. The maximum in each of dM/dH curves indicates the transition from the antiferromagnetic to paramagnetic phase. Based on the above measurements, a tentative H–T phase diagram for $CeAu_2Si_2$ for $M_{\|c}$ is constructed (Fig. 18c).

4. Conclusions

Motivated by properties of the rare-earth transition-metal silicide family RT_2Si_2, we have grown $CeAu_2Si_2$ and $CeAu_4Si_2$ crystals and confirmed their structures. In the 1:4:2 structure there are, contrary to 1:2:2, bilayers of gold along [010] direction. The $CeAu_2Si_2$ $I4/mmm$ structure with $a = 4.3072(6)$ Å and $c = 10.196(2)$ Å, is found to be stoichiometric. The $CeAu_4Si_2$ phase crystallizes in $Cmmm$ structure with $a = 4.316(2)$ Å, $b = 13.741(8)$, and $c = 4.350(2)$ Å, different from a reported tetragonal result [23]. The physical properties of $CeAu_4Si_2$ phase here are different enough from that reported ($P\bar{4}m2$) [23] to support their difference in space groups.

Although both $CeAu_2Si_2$ and $CeAu_4Si_2$ have similar structural stacking, they present unique magnetic features. $CeAu_4Si_2$ possesses a ferromagnetic component below 3.3 K, and another transition at 1.85 K. On the other hand, $CeAu_2Si_2$ is a typical antiferromagnet with $T_N = 8.8(1)$ K. For $CeAu_2Si_2$, we suspect that a small component of ferromagnetic impurity, consistent with a $CeSi_{1.84}$ phase [35], is only observed in $M(T, H)$ data (Fig. 17).

In the two cerium gold silicides, because of the localized character of the 4f moments, the RKKY indirect exchange interaction is expected to be the dominating factor for their low temperature magnetic behaviors. The intersite interaction temperature T_{RKKY} is subject to $J_{sf}^2 N(E_f)$ term and the strength of J_{sf} is dependent on the volume and electronic effects. For $CeAu_2Si_2$, the magnetic structure [1] consists of alternating ferromagnetic layers, with the moments perpendicular to the layers, believed to be the characteristic of 4f–4f interactions mediated through hybridization with conduction electrons. Here, the unit

cell volume is 189.15(5) Å^3. In isostructural families, the larger the unit cell volume, the smaller is the 4*f*-conduction electron overlap giving rise to a decrease in the magnitude of J_{sf}. However, the comparison of 1:2:2 and 1:4:2 phases with different symmetries is not easy. The unit cell volume for $CeAu_4Si_2$ is naturally larger 259.3(6) Å^3, with bilayers of distorted tetragonal antiprisms separated by twin gold layers. The estimated Debye temperatures for $CeAu_4Si_2$ and $CeAu_2Si_2$ are $\theta_D \approx 85$ and 110 K, respectively. With a small deviation in lattice excitations, the strong differences in $C(T)$ at low temperatures (Figs. 8 and 13) may be mainly due to variations in the electronic spectrum. Band structure calculations are needed to find the true nature of interactions and distinctions between the two phases.

For both compounds, the fits of the high temperature magnetization data to Curie–Weiss give evidence of ferromagnetic and antiferromagnetic interactions along easy and hard magnetization axes, respectively (Table 4). The polycrystalline average of the effective paramagnetic moment is useful as it minimizes the crystal electric field effects and are, for $CeAu_4Si_2$ and $CeAu_2Si_2$, 2.65 and 2.49 μ_B/Ce, respectively. The effective moments are close in value to the corresponding free rare-earth cerium ion (2.54 μ_B/Ce). The magnetization value at 70 kOe and 1.8 K in both samples is $\sim$1.3 μ_B (Table 4), small compared with the free Ce^{3+} value.

There is no indication for a Kondo effect in the presence of magnetic order in either phase. First, there is no evidence for a sizable linear specific-heat term γT (Figs. 9a and 14a) as $\gamma = 10(2)$ and 21(1) mJ/K^2 mol, respectively for $CeAu_4Si_2$ and $CeAu_2Si_2$ compounds, suggesting little to no correlated electron behavior. Second, the total entropy associated with the specific heat anomaly at magnetic ordering temperature is $\sim R \ln 2$ for both samples (Figs. 9b and 14b), suggesting that the $J = 5/2$ multiplet of the Ce^{3+} ion is split into three Kramers doublets in the 4*f* crystal electric field scheme. For $CeAu_2Si_2$, evidence of a low T_K (1.7 K) was found earlier, from zero-temperature value of the quasielastic linewidth in the magnetic neutron scattering [17]. For $CeAu_2Si_2$, the reported moment determined by a neutron diffraction experiment at 5 K is 1.29(5) μ_B, again less than full Ce^{3+} moment [1]. Therefore in both samples, the $M(H)$ reduced saturated moment may be due to crystal field effects.

Acknowledgment

Work at the Ames Laboratory was supported by the Department of Energy-Basic Energy Sciences under Contract no. DE-AC02-07CH11358.

Appendix A. Supplementary data

CIF files for the three refined structures can be obtained from the Fachinformationszentrum Karlsruhe, 76344 Eggenstein-Leopoldshafen, Germany (fax: (49) 7247-808-666; e-mail: crysdata@fiz.karlsruhe.de) on quoting the Registry Nos. CSD–418530 ($CeAu_2Si_2$), CSD–418529 ($CeAu_4Si_2$), and CSD–418531 ($Ce_{0.93}Au_4Si_2$).

References

[1] B.H. Grier, J.M. Lawrence, V. Murgai, R.D. Parks, Phys. Rev. B 29 (1984) 2664.
[2] C.S. Garde, J. Ray, J. Phys.: Condens. Matter 6 (1994) 8585.
[3] G.F. Von Blanckenhagen, G.R. Stewart, Solid State Commun. 108 (1998) 535.
[4] Y. Kawasaki, K. Ishida, Y. Kitaoka, K. Asayama, Phys. Rev. B 58 (1998) 8634.
[5] S.K. Malik, D.T. Adroja, Phys. Rev. B 43 (1991) 6295.
[6] K.D. Myers, S.L. Bud'ko, I.R. Fisher, Z. Islam, H. Kleinke, A.H. Lacerda, J. Magn. Magn. Mater. 205 (1999) 27.
[7] D.T. Adroja, B.D. Rainford, S.K. Malik, Physica B 186–188 (1993) 566.
[8] C.L. Lin, T. Yuen, P. Riseborough, X.-Y. Huang, J. Li, J. Appl. Phys. 91 (2002) 8117.
[9] S.K. Dhar, S.M. Pattalwar, R. Vijayaraghavan, Physica B 186–188 (1993) 491.
[10] R. Pöttgen, H. Borrmann, R.K. Kremer, J. Magn. Magn. Mater. 152 (1996) 196.
[11] I. Mayer, J. Cohen, I. Felner, J. Less-Comm. Met. 30 (1973) 181.
[12] S. Doniach, Physica B 91 (1977) 231.
[13] L.C. Gupta, D.E. MacLaughlin, C. Tien, C. Godart, M.A. Edwards, R.D. Parks, Phys. Rev. B 28 (1983) 3673.
[14] J.D. Thompson, R.D. Parks, H. Borges, J. Magn. Magn. Mater. 54–57 (1986) 377.
[15] A. Amato, J. Sierro, J. Magn. Magn. Mater. 47–48 (1985) 526.
[16] F. Steglich, J. Aarts, C.D. Bredl, W. Lieke, D. Meschede, W. Franz, H. Schäfer, Phys. Rev. Lett. 43 (1979) 1892.
[17] A. Severing, E. Holland-Moritz, B. Frick, Phys. Rev. B 39 (1989) 4164.
[18] T. Fujiwara, M. Sugi, N. Kimura, I. Satoh, T. Komatsubara, H. Aoki, Phys. B: Conden. Matter 378–380 (2006) 812.
[19] F. Honda, J. Vejpravova, P. Svoboda, V. Sechovsky, G. Oomi, T. Komatsubara, J. Magn. Magn. Mater. 272–276 (2004) E409.
[20] E. Santava, J. Vejpravova, F. Honda, T. Komatsubara, V. Sechovsky, J. Magn. Magn. Mater. 310 (2007) e586.
[21] I. Felner, J. Phys. Chem. Sol. 36 (1975) 1063;
T.T.M. Palstra, A.A. Menovsky, G.J. Nieuwenhuys, J.A. Mydosh, J. Magn. Magn. Mater. 54 (1986) 435.
[22] E. Heeb, H.R. Ott, E. Felder, F. Hulliger, A. Schilling, Z. Fisk, Solid State Commun. 77 (1991) 323.
[23] H. Nakashima, A. Thamizhavel, T.D. Matsuda, Y. Haga, T. Takeuchi, K. Sugiyama, R. Settai, Y. Onuki, J. Alloys Compds. 424 (2006) 7.
[24] O.I. Bodak, E.I. Gladyshevskii, V.K. Pecharskii, Kristallografiya 22 (1977) 178.
[25] P.C. Canfield, Z. Fisk, Philos. Mag. B 65 (1992) 1117.
[26] M.G. Kanatzidis, R. Pöttgen, W. Jeitschko, Angew. Chem. Int. Ed. 44 (2005) 6996.
[27] SMART: Bruker AXS, Inc., Madison, W1, 1996.
[28] SHELXTL: Bruker AXS, Inc., Madison, WI, 2000.
[29] P. Boutron, Phys. Rev. B 7 (1962) 1731.
[30] B.D. Dunlap, J. Magn. Mag. Mater. 37 (1983) 211.
[31] A. Arrott, Phys. Rev. 108 (1957) 1394.
[32] M.E. Fisher, Philos. Magn. 7 (1962) 1731.
[33] M.E. Straumanis, J. Mater. Sci. 23 (1988) 757.
[34] U. Häussermann, S. Amerioun, L. Eriksson, C.-S. Lee, G.J. Miller, J. Am. Chem. Soc. 124 (2002) 4371.
[35] S.A. Shaheen, J.S. Schilling, Phys. Rev. B 35 (1987) 6880.
[36] L. Pauling, Nature of the Chemical Bond, third ed, Cornell University Press, Ithaca, NY, 1960.